GEOPHYSICS, VOL. 75, NO. 6 (NOVEMBER-DECEMBER 2010); P. I51–I58, 6 FIGS., 2 TABLES.
10.1190/1.3506559

# Euler deconvolution of gravity anomalies from thick contact/fault structures with extended negative structural index

Petar Stavrev[1] and Alan Reid[2]

## ABSTRACT

The concept of extended Euler homogeneity of potential fields is examined with respect to all variables of length dimension in their analytical expressions. This reveals the possible existence of positive degrees of homogeneity or corresponding negative structural indices considered as extensions of the Thompson's structural indices in Euler deconvolution. This approach is implemented for a contact gravity model, represented by a 2D semi-infinite slab with large thickness relative to its depth. Applying Euler deconvolution on synthetic and field data indicates that the positive degree of homogeneity, i.e., the extended negative structural index, is the appropriate one for the inversion of gravity anomalies from contact structures.

## INTRODUCTION

Conventional Euler deconvolution (Reid et al., 1990) of gravity and magnetic data estimates the spatial position and shape type of sources by assuming interpretation models of one singular point. One-point sources have their position described by a single spatial location, e.g., the sphere center, the thin rod top or sheet edge, the axis of an infinite circular cylinder, or the infinite contact top corner. The source coordinates and the shape index, known as "structural index (SI) $N''$ (after Thompson, 1982), are coefficients in Euler's differential equation for homogeneous functions of degree $n = -N$. This equation enables practical inversions of massive data sets. Various inversion techniques have been proposed and implemented in practice, (e.g., Thompson, 1982; Reid et al., 1990; Stavrev, 1997; Barbosa et al., 1999; Zhang et al., 2000; Nabighian and Hansen, 2001; Gerovska and Arauzo-Bravo, 2003; Salem and Ravat, 2003; Mushayandebvu et al., 2004; Reid et al., 2003). They all apply positive or zero SIs following Thompson's (1982) functional form for one-point sources.

The theoretical analysis of Euler homogeneity as a fundamental property of potential fields (Stavrev, 1997; Stavrev and Reid, 2007) leads to the prediction of negative SIs for some interpretation models that have a positive degree of Euler homogeneity. One such model is the vertical component of gravity field of a contact with considerable thickness relative to its depth.

Euler homogeneity and its degree for a potential field can be tested using the definition for homogeneous functions (e.g., Courant and John, 1965):

$$f(t\mathbf{v}) = t^n f(\mathbf{v}), \tag{1}$$

or Euler's differential equation derived from equation 1,

$$\mathbf{v}\nabla f(\mathbf{v}) = nf(\mathbf{v}), \tag{2}$$

where $\mathbf{v} = (v_1, v_2, \ldots, v_k)$ is the set (vector) of an arbitrary number $k$ of variables (components) with respect to which the homogeneity of the field $f$ is tested; $t$ is a real number, accepted here as a scaling factor $> 1$; and $n$ is the degree of homogeneity of $f(\mathbf{v})$. Stavrev and Reid (2007) show that a potential field possesses homogeneity with respect to the set of variables $\mathbf{v}$, which includes all quantities with length dimension in the field analytical expression, rather than just the coordinates of observation points; thus, interpretation models of several singular points can be treated as complicated homogeneous models and, in some cases, converted to one-point models. This concept of extended generalized homogeneity provides wider possibilities for field inversions using equations 1 and 2.

In this paper, we apply the property of extended homogeneity to Euler deconvolution of gravity anomalies from contact structures. We test the method on synthetic models of different depth extent with positive degree $n = 1$, i.e., using an equivalent negative SI, $N = -1$. The latter is not in agreement with Thompson's (1982) explanation of the physical sense of this term, related to the different "rate of decay" of the field with distance from its one-point source. We show that the term "structural index" can be extended from the

Manuscript received by the Editor 21 July 2009; revised manuscript received 12 February 2010; published online 18 November 2010.
[1]University of Mining and Geology "St. Ivan Rilski," Department of Applied Geophysics, Sofia, Bulgaria. E-mail: pstavrev@mail.bg.
[2]School of Earth and Environment, University of Leeds, United Kingdom; and Reid Geophysics, Eastbourne, United Kingdom. E-mail: alan@reid-geophys.co.uk.

simplest one-point sources to sources with two singular points, keeping at the same time a clear physical and geometric sense for this term; thus, we relate this index to the field property of Euler homogeneity used directly for the field deconvolution. A field example supported well by data demonstrates the inversion procedures and proves the positive degree of Euler homogeneity or the extended negative SI to be appropriate for gravity anomalies from contact structures with considerable thickness.

## THEORETICAL NOTES

Consider a contact gravity model as a 2D semi-infinite horizontal layer with constant density contrast, limited by a vertical or inclined surface (contact). The vertical component, $g$, of gravity anomaly from a vertical contact (Figure 1) is

$$g = \gamma\rho\{\pi(z_2 - z_1) + 2(z_2 - z)\tan^{-1}[(x - x_0)/(z_2 - z)] - 2(z_1 - z)\tan^{-1}[(x - x_0)/(z_1 - z)] + \ln\{[(x - x_0)^2 + (z_2 - z)^2]/[(x - x_0)^2 + (z_1 - z)^2]\}\ (x - x_0), \qquad (3)$$

where $\gamma$ is the gravitational constant, $\rho$ is the density contrast, $(x,z)$ are the coordinates of observation points $P$, and $(x_0,z_1)$ and $(x_0,z_2)$ are the coordinates of the upper and lower edge points of the contact (semi-infinite slab, Telford et al., 1990), respectively.

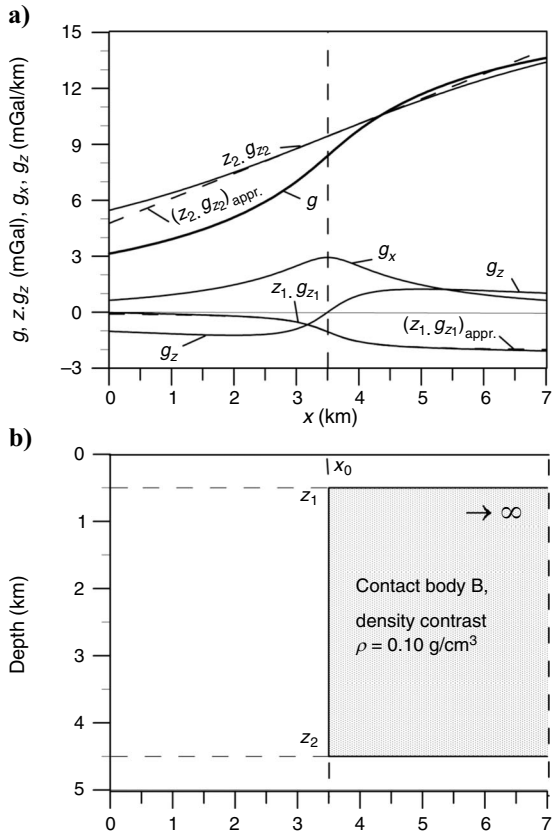


Figure 1. Gravity vertical contact model. (a) Profiles of anomalous gravity intensity $g$ and its horizontal gradient $g_x$ and vertical gradient $g_z$; profiles of the terms $(z_1.g_{z1})$ and $(z_2.g_{z2})$ in Euler's differential equation 5 and their approximations $(z_1,g_{z1})_{appr.}$ and $(z_2.g_{z2})_{appr.}$, substituted in equation 8. (b) Vertical cross section of the source body B of a vertical contact structure with density contrast $\rho = 0.1$ g/cm$^3$.

We can do a simple test of homogeneity of expression 3 with equation 1 by applying a scaling factor $t$ to all variables of length dimension $\mathbf{v} = (x,z,x_0,z_1,z_2)$. This shows that $g(t\mathbf{v}) = tg(\mathbf{v})$ and, hence, the degree of homogeneity $n = 1$; therefore, the SI should be $N = -1$ (Stavrev and Reid, 2007). This result points to the fact that the scaled field $g' = g(x',z',x_0',z_1',z_2')$, where $x' = tx$, $z' = tz$, $x_0' = tx_0$, $z_1' = tz_1$, $z_2' = tz_2$ is $t$ times greater than the original field $g(x,z,x_0,z_1,z_2)$, i.e., $g'(P') = tg(P)$, or $g' > g$ when $t > 1$. The analytical expression for $g'$ is the same equation 3, valid for the field $g$, but $g'$ arises from an increase in the vertical size of the scaled source, contact body $\mathbf{B}' = t\mathbf{B}$ (Figure 2), having the same density $\rho$; thus, the positive degree of homogeneity $n = 1$ or respective negative SI $N = -1$ does not violate Newton's law of gravitation. The transform $g' = tg$ used here reflects the radial geometric transform $\mathbf{B}' = t\mathbf{B}$ with respect to the origin of a chosen coordinate system or other point, known as a central point of similarity with coefficient $t$. The effect on a source body is shown in Figure 2. The difference between the original and scaled

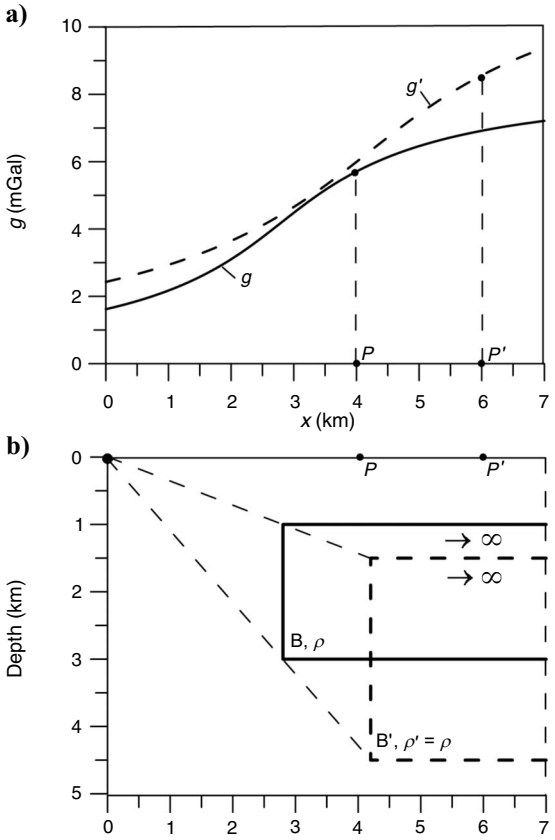


Figure 2. Original and transformed gravity contact model according to the expression 1 of homogeneity for degree $n = 1$ (or corresponding SI $N = -1$) and scaling coefficient $t = 1.5$. (a) Gravity profiles: $g$ from the original source; $g'$ from the equivalent transformed source, $g'(P') = tg(P)$, where at the observation point $P$ with abscissa $x = 4$ km the gravity intensity $g(P) = 5.710$ mGal, whereas at point $P'$ with abscissa $x' = 1.5x = 6$ km, the calculated $g'(P') = 8.565$ mGal, i.e., $g'(P') = 1.5 \times 5.710$ mGal. (b) Gravity model sources: original source, contact body B, and its transformed image, contact body $\mathrm{B}' = t\mathrm{B}$, generated from the origin (0, 0) of the coordinate system. The density contrast of the two bodies is $\rho = 0.1$ g/cm$^3$.

fields at points $P'$ forms the finite-difference similarity transform, and when $t \to 1$, it forms the differential similarity transform (Stavrev, 1997).

The aforementioned behavior of value and sign and the physical and geometric sense of the degree of homogeneity $n$ follow from the reformulated equation 1,

$$n = \ln[f(t\mathbf{v})/f(\mathbf{v})]/\ln t, \tag{4}$$

valid for $t > 0$, including for $t = 1$. If we accept the relationship $N = -n$, then the equation 4 gives results in agreement with Thompson's (1982) SIs $N$ for all one-point models. For more complicated models, Thompson's functional form $f = G/r^N$, containing constant $G$, and inverse distance from observation points to one-point source, i.e., $r$ with exponent $N$, cannot explain negative SIs or the corresponding positive degrees of Euler homogeneity. Models such as our contact model with two singular points can be tested for their degree of homogeneity $n$ or the corresponding SI $N = -n$ using equation 1 and 2, or 4 (equation 1 is easiest) over the analytical expression such as 3 of the model field.

An interpretation model consists of two related parts: The source and the field created. The use of the term "structural index" underlines the source type, whereas the term "degree of homogeneity" emphasizes a field property. The latter term is preferred in theoretical analyses. In the practice of interpretation of data, the term "structural index" prevails. so we use either term depending on the case; however, to distinguish the negative SIs from the usually nonnegative ("single point") ones, we propose the term "extended" SIs according to the concept of extended Euler homogeneity.

For the gravity contact model, Euler's differential equation 2 takes the form

$$x\partial g/\partial x + z\partial g/\partial z + x_0\partial g/\partial x_0 + z_1\partial g/\partial z_1 + z_2\partial g/\partial z_2 = ng, \tag{5}$$

where $n = -N = 1$. Equation 5 contains the unknown coordinates $x_0$, $z_1$, and $z_2$ and the unknown derivatives $\partial g/\partial z_1$ and $\partial g/\partial z_2$. This is a nonlinear equation with respect to the unknowns. It is possible to invert data $g$ to obtain the coordinates $x_0$, $z_1$, and $z_2$ using differential similarity transforms (Stavrev, 1997). Another, more direct way to solve the inverse problem is to use approximations for terms that contain the unknown derivatives. Stavrev and Reid (2007) propose the following substitutions:

$$z_1\partial g/\partial z_1 = -z_1\partial g/\partial z - [\pi\gamma\rho z_1 + 2\gamma\rho(z_1/z_2)(x - x_0)] \tag{6}$$

$$z_2\partial g/\partial z_2 = [\pi\gamma\rho z_2 + 2\gamma\rho(x - x_0)], \tag{7}$$

when $z_2 \gg z_1$ and $|x - x_0| \ll z_2$, (equations 29 and 30 of Stavrev and Reid, 2007). Figure 1 illustrates the nearness of these approximations to the correct terms in equation 5 for $z_2 = 9z_1$. If we recast equation 5 by substituting 6 and 7 and exploiting $\partial g/\partial x_0 = -\partial g/\partial x$, then we obtain

$$\begin{aligned} x_0\partial g/\partial x + z_1\partial g/\partial z - [\pi\gamma\rho(z_2 - z_1) + 2\gamma\rho(x - x_0)] \\ = -ng + x\partial g/\partial x + z\partial g/\partial z, \end{aligned} \tag{8}$$

where on the left-hand side, the unknown coordinates $x_0$ and $z_1$ are multiplied by the measured or calculated gradients $\partial g/\partial x$ and $\partial g/\partial z$ and form the bracketed term as a linear function of $x$ along with the unknowns $z_2$ and $\rho$. Euler's equation 5 is reduced to equation 8, focusing the solution on the upper edge point of the contact structure. In addition, we may find its thickness $(z_2 - z_1)$ and density contrast $\rho$.

A sloping-contact model has the complicated field expression (Telford et al., 1990)

$$\begin{aligned} g = 2\gamma\rho\{\pi(z_2 - z_1)/2 + (z_2\theta_2 - z_1\theta_1) \\ + x[(\theta_2 - \theta_1)\sin\beta\cos\beta + \cos^2\beta\ln(r_2/r_1)]\}, \end{aligned} \tag{9}$$

where $r_1^2 = (x - a_1)^2 + z_1^2$, $r_2^2 = (x - a_2)^2 + z_2^2$; $a_1$ and $a_2$ are the horizontal coordinates of the upper and lower edge points, respectively; and $\theta_1$, $\theta_2$, and $\beta$ are dimensionless angles. The quantities of length dimension $x$, $z_1$, $z_2$, $a_1$, and $a_2$ define degree of homogeneity $n = 1$.

## METHODS

Consider the observed gravity anomaly $\Delta g$ created by a vertical contact as a sum of the contact-structure anomaly $g$ and a constant background field $b$, i.e., $\Delta g = g + b$. Equation 8 at a given observation point with coordinates $(x_i, z_i)$ becomes

$$\begin{aligned} (\partial\Delta g/\partial x)_i x_0 + (\partial\Delta g/\partial z)_i z_1 + (-2\gamma x_i)\rho \\ + [2\gamma\rho x_0 - \pi\gamma\rho(z_2 - z_1) - nb] \\ = -n\Delta g_i + x_i(\partial\Delta g/\partial x)_i + z_i(\partial\Delta g/\partial z)_i, \\ i = 1,2,\ldots L, \end{aligned} \tag{10}$$

where $L$ is the number of observation points, and $n = -N = 1$. The unknown quantities in equation 10 are $u_1 = x_0$, $u_2 = z_1$, $u_3 = \rho$, and $u_4 = 2\gamma\rho x_0 - \pi\gamma\rho(z_2 - z_1) - b$. If $L > 4$ (usually $L \gg 4$), then an overdetermined system of equation 10 can be composed and solved by a least-squares method as is normally done in Euler deconvolution. The mixed unknown $u_4$ contains the term $\pi\gamma\rho(z_2 - z_1) = T/2$, where $T$ is the amplitude of the contact anomaly $g$. The value of $T/2$ appears at a point with abscissa $x_0$ (Telford et al., 1990), thus the sum

$$\pi\gamma\rho(z_2 - z_1) + b = \Delta g(x_0), \tag{11}$$

which can be taken from the gravity profile at $x_0$. If depth $z_1$ and density contrast $\rho$ are estimated, then depth to the lower contact edge is $z_2 = z_1 + (T/2)/\pi\gamma\rho$.

The inverse problem of the contact model may be completely solved for all of its parameters $x_0$, $z_1$, $z_2$, and $\rho$, but the result is not stable, irrespective of the method used. This is because vertical contacts with different thickness but equal value of $\rho(z_2 - z_1)$ create similar anomalous fields that have the same values at point $x_0$ (Figure 3; equation 11). There is coupling between the density contrast $\rho$ and thickness $(z_2 - z_1)$ in equation 10. For stabilization of the solution, additional information or requirements must be included (Tikhonov and Arsenin, 1977; Zhdanov, 2002). For example, constraints on the values of some unknowns, such as the coordinate $x_0$ or the density $\rho$, can be imposed to form a compact set of the source model parameters.

The linear bracketed term [.] in equation 10 can be eliminated by differentiating with respect to the variable $x$; thus, we form the equations

$$\begin{aligned} (\partial^2\Delta g/\partial x^2)_i x_0 + (\partial^2\Delta g/\partial z\partial x)_i z_1 + (-2\gamma)\rho = x_i(\partial^2\Delta g/\partial x^2)_i \\ + z_i(\partial^2\Delta g/\partial z\partial x)_i, \quad i = 1,2,\ldots L, \end{aligned} \tag{12}$$

which is a linear set of equations for the three unknowns $x_0$, $z_1$, and $\rho$.

The price for this simplification is the possible increase of noise-to-signal ratio because the second derivatives are now included.

The contact horizontal position $x_0$ coincides with the point of maximum (or minimum for $\rho < 0$) horizontal derivative $\partial\Delta g/\partial x$ and with the point of zero vertical derivative $\partial\Delta g/\partial z$ (Figure 1). This point is easily determined visually or numerically. If we treat $x_0$ as a known quantity, then from equations 10 and 11

$$(\partial\Delta g/\partial z)_i z_1 + [2\gamma(x_0 - x_i)]\rho = -\Delta g(x_i) + \Delta g(x_0) + (x_i - x_0)(\partial\Delta g/\partial x)_i + z_i(\partial\Delta g/\partial z)_i, \quad i = 1,2,\ldots L. \tag{13}$$

Equations 12 and 13 suffer from the same coupling effects as equation 10, but if the density contrast $\rho$ or its range is known from other work, then the depth $z_1$ or its range can be estimated from these equations. A direct solution for $z_1$ follows from equation 13:

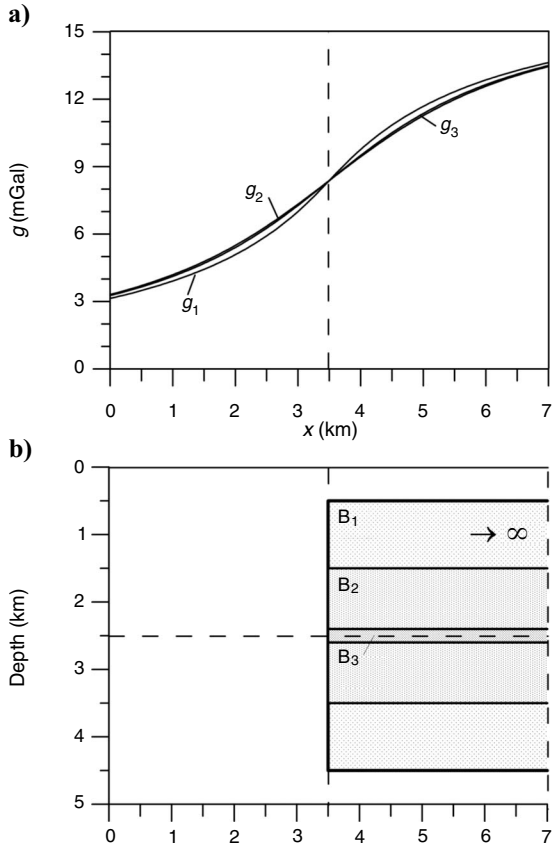


Figure 3. Gravity contact models of close anomalous fields created by contact structures of different parameters but equal product $\rho(z_2 - z_1)$ of their density contrast $\rho$ and amplitude $\Delta z = (z_2 - z_1)$. (a) Profiles of anomalous gravity intensity $g$, numbered according to the number of their sources. (b) Vertical cross section of contact structures with common depth to midpoint of 2.5 km but different density contrast $\rho$ and amplitude $\Delta z$: contact body $B_1$ with $\rho_1 = 0.1$ g/cm$^3$ and $\Delta z_1 = 4$ km so that $\rho_1\Delta z_1 = 0.4$; contact body $B_2$ with $\rho_2 = 0.2$ g/cm$^3$ and $\Delta z_2 = 2$ km so that $\rho_2\Delta z_2 = 0.4$; contact body $B_3$ with $\rho_3 = 2$ g/cm$^3$ and $\Delta z_3 = 0.2$ km so that $\rho_3\Delta z_3 = 0.4$. The product $\rho\Delta z$ has the dimension of surface density of mass, in SI units equal to $0.4 \times 10^6$ kg/m$^2$ for the three contacts.

$$(z_1)_i = [\Delta g(x_0) - \Delta g(x_i) + (x_i - x_0)(\partial\Delta g/\partial x)_i + z_i(\partial\Delta g/\partial z)_i + 2\gamma(x_i - x_0)\rho]/(\partial\Delta g/\partial z)_i, \quad i = 1,2,\ldots L, \tag{14}$$

which is valid at data points $i$ around $x_0$, $(x_i \neq x_0)$.

A suitable choice of data windows is necessary for stable solutions from all equations discussed. Windows must cover the intervals of interpreted profile where the data are sensitive to the unknowns. The sensitivity is $S_{ij} = \partial(Au)_i/\partial u_j$, where $A$ is the matrix of equation sets 10, 12, or 13 with the common operational equation $Au = d$, where $u$ is the set of the unknowns and $d$ is the set of the right-hand side of these equations that contain data. After differentiating equation 10, we obtain the following results for the unknowns $x_0$ and $z_1$:

$$\partial(Au)_i/\partial x_0 = (\partial\Delta g/\partial x)_i \text{ and } \partial(Au)_i/\partial z_1 = (\partial\Delta g/\partial z)_i.$$

An analysis of these results points to preferred windows centered at the point $x_0$ of the horizontal gradient extremum, covering the interval between vertical-gradient extremes. In addition, the coefficients $(-2\gamma x_i)$ in equation 10 and $-2\gamma(x_i - x_0)$ in equation 13 form linear functions of the observation coordinates $x$. If the vertical-gradient curve were taken in a short window around center $x_0$, where it is close to a linear function (see the model example in Figure 1 and the real field example in Figure 6 below), then this would destabilize the solution, so the size of a data window depends on the distance between the vertical-gradient extremes and the necessary number of data points. The maximum window half-length should be less than the assumed depth to the lower edge point of the contact structure (inequalities 6 and 7).

Figure 3 shows the closeness of anomalous fields from contact type sources. This makes it difficult to recognize their thickness so that a suitable approach to the data interpretation can be chosen. The thick contact model has an extended SI equal to $-1$, whereas a thin semi-infinite sheet, approximating a small gravity step, has SI equal to 0. The latter case should be resolved by direct application of Euler's differential equations,

$$(\partial\Delta g/\partial x)_i x_0 + (\partial\Delta g/\partial z)_i z_0 = x_i(\partial\Delta g/\partial x)_i + z_i(\partial\Delta g/\partial z)_i, \quad i = 1,2,\ldots L, \tag{15}$$

where $(x_0, z_0)$ are coordinates of the thin step (sheet) edge. The contact's thickness can be estimated by the ratio $z_2/z_1$, which along with the density contrast $\rho$ defines the $(\partial\Delta g/\partial x)$ extreme value, $|\partial\Delta g/\partial x|_e = 2\gamma\rho \ln(z_2/z_1)$. Using symbol $p = z_2/z_1$,

$$p = \exp[|\partial\Delta g/\partial x|_e/2\gamma\rho]. \tag{16}$$

This estimation needs the density $\rho$ or its possible range $(\delta\rho)$ to be known. If this range is relatively small around a given density $\rho$, then $(\delta p)/p = -(\ln p)(\delta\rho)/\rho$, following the derivative of equation 16 with respect to $\rho$. The model tests shown in the next section help the interpreter to distinguish the thin from the thick contact and to use equations 10–14 or equation 15 for Euler deconvolution of gravity anomalies of transition type (Figures 1, 3, 5, and 6).

The case of a sloping-contact model, equation 9, can be resolved by the same but more complicated inverse procedures, including similarity transforms. It needs additional deductions and approximations that go beyond the purpose of this paper.

Note that if we use practical measurement units mGal for $\Delta g$, km for the coordinates, and g/cm$^3$ for the density, then coefficient $\gamma$ has the value of 6.672 in all equations already mentioned and tests in the next section.

## MODEL TESTS

1) The contact models shown in Figure 3 are tested with our implementation of Euler deconvolution using two SIs, $N = -1$ and $N = 0$, and the appropriate set of equations for thick and thin contacts. The results shown in Figure 4 verify the proposed inversion technique with negative SI and indicate its effectiveness in the case of relative thickness $z_2/z_1 > 4$. For relatively thin contacts, the use of conventional Euler deconvolution with SI $N = 0$ is more appropriate, but this index used in case of thick contacts gives a depth $z_0$ from equation 15 quite different from the depth to midpoint $(z_1 + z_2)/2$ of the thick contact.
2) A set of contact models is tested with respect to their thickness, different length of windows, noise added, and equations applied for the gravity field deconvolution. We use a vertical contact model defined in relative units (r.u.) to the depth $z_1$ of the upper edge point of the contact. Then, the level $z$ of the calculated anomaly takes the value of 0, the depth $z_1 = 1$ r.u. (1 km, 1 hm = 100 m, or another unit of length), the horizontal location is $x_0 = 0$, and the data point spacing is $\Delta x/z_1 = 0.2$ r.u.. The density contrast is $\rho = 0.1$ g/cm$^3$. Variable parameters are the depth ratio $p = z_2/z_1$, the window length $W/z_1$, the regional field $b$, and standard deviation $s$ of a random noise added.

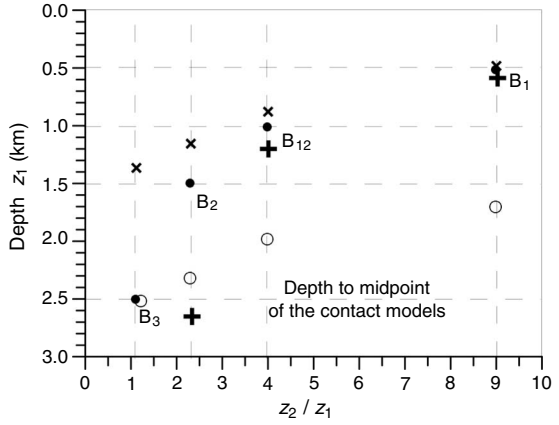


Figure 4. Comparative depth estimates of the contact models from Figure 3 for different relative parameters of the contacts $z_2/z_1$ (ratio of depth $z_2$ of the lower edge point to depth $z_1$ of the upper edge point). Symbols: ●, exact depth $z_1$; ×, estimated depth $z_1$ using proposed Euler deconvolution from set of equations 10 with extended SI $N = -1$; +, estimated depth $z_1$ from equation 14 with given coordinate $x_0$ of the edge point and value of $g_a$ anomaly at point $x_0$ and assumed density $\rho$ as input; ○, estimates of the depth $z_0 = (z_1 + z_2)/2$ of the contact using conventional Euler deconvolution from set of equations 15 with SI $N = 0$. Letters $B_1$, $B_2$, $B_3$, and intermediate $B_{12}$ show the upper edge points of the contact models, all of them with a common midpoint depth of 2.5 km.

Models vary from a considerable thickness of $z_2/z_1 = 20$ to a moderate contact thickness at $z_2/z_1 = 5$. The window length is tested from a minimum of $W/z_1 = 1.2$ to a length equal to the half-depth $z_2/z_1$; thus, the conditions for the substitutes 6 and 7 are satisfied so that $z_2 > 5z_1$ and $|x - x_0| < 0.25z_2$.

Results from the model tests are shown in Table 1. Equation sets 10 and 13 and equation 14, constructed with the prescribed degree $n = 1$, equivalent to the negative SI $N = -1$, give solutions close to the input model parameters. The coordinates $x_0$ and $z_1$ of the upper edge point of a contact with a considerable depth extent are obtained from these equations with proper selections of ratio $z_2/z_1$ and ratio $W/z_2$. When $z_2/z_1 \geq 5$ and $W/z_2 \leq 0.25$, the deviation in the estimated depth $z_1$ is $< 5\%$. In all tested models, the estimated depth $z_1$ from systems 10 and 13 is less than the true one, whereas from the direct equations 14, it is greater. The density contrast $\rho$ can be found but with low accuracy (error up to 25%). The estimated densities are less than the true density. This demonstrates the compensation effect between the estimated density $\rho$ and estimated thickness $\Delta z = (z_2$

**Table 1. Estimated depth $z_{1e}$ and position $x_{0e}$ of the upper edge point of contact models with different depth extent, $z_2$, and estimated density contrast $\rho_e$ from equations 10, 13, and 14.**

| Depth $z_2/z_1$ | Window length $W/z_1$ | Window half-length $(W/2)/z_2$ | $x_{0e}$ (km) ($x_0 = 0.0$) | $z_{1e}$ (km) ($z_1 = 1.0$) | $\rho_e$ (g/cm$^3$) ($\rho = 0.10$) | $u_4$ (mGal) | $z_{1e}$ (equation 14), Noise $b$, $s$ (mGal) |
|---|---|---|---|---|---|---|---|
| 20.0 | 1.0 | 0.025 | 0.004 | 0.997 | 0.095 | − 39.84 | $z_{1e} = 1.056$ |
| | 5.0 | 0.125 | 0.000 | 0.987 | 0.094 | − 39.83 | |
| | 5.0 | 0.125 | 0.000 | 0.987 | 0.094 | − 29.83 | $b = -10.000$ |
| | 5.0 | 0.125 | − 0.018 | 1.003 | 0.096 | − 39.79 | $s = \pm 0.025$ |
| | 10.0 | 0.250 | 0.000 | 0.954 | 0.092 | − 39.83 | |
| 10.0 | 1.0 | 0.050 | 0.000 | 0.991 | 0.089 | − 18.86 | $z_{1e} = 1.117$ |
| | 5.0 | 0.250 | 0.000 | 0.953 | 0.087 | − 18.87 | |
| | 5.0 | 0.250 | 0.008 | 0.967 | 0.088 | − 18.82 | $s = \pm 0.025$ |
| 5.0 | 1.0 | 0.100 | 0.000 | 0.961 | 0.077 | − 8.38 | $z_{1e} = 1.267$ |
| | 2.0 | 0.200 | 0.000 | 0.945 | 0.076 | − 8.38 | |
| | 2.0 | 0.200 | 0.000 | 0.945 | 0.076 | − 28.38 | $b = 20.000$ |

The results for $z_{1e}$ from equation 13 coincide with those from equation 10 at $x_0 = 0$ as input. The results shown for $z_{1e}$ from equation 14 correspond to $x_0 = 0$ and $\rho = 0.10$ g/cm$^3$. $b$, regional field as a systematic noise; $s$, standard of the random noise for the row.

$-z_1$), which increases as $z_1$ decreases. The constant value of $u_4$, in all tests at given depth $z_2/z_1$ and constant field $b$, reflects the same effect; however, the models show that the existence of a constant regional field $b$ in the gravity data does not affect the solution from the proposed deconvolution.

## FIELD EXAMPLE: VENELIN-AKSAKOV FAULT IN THE DOLNA KAMCHIA DEPRESSION

The Dolna (lower) Kamchia depression lies in Eastern Bulgaria along the lower course of the Kamchia river. This depression is elongated west to east and runs into the adjoining Black Sea shelf, according to geophysical data (Dachev, 1988). It belongs geologically to the most northeastern part of the Balkan orogenic system (Dabovski et al., 2002). Thick Paleogene and Neogene sediments filled the depression to a depth of 3.6 km above Cretaceous layers, reached in onshore wells.

The Venelin-Aksakov fault is the western bound of the depression. An intense gravity gradient zone (Figures 5 and 6) indicates a steep contact structure with north-to-south orientation. Exploratory wells (Figure 5) west and east of the line of the gravity gradient zone indicate a considerable difference in the depth to the boundary between the low-density tertiary-upper Cretaceous layers and the denser lower Cretaceous and deeper sediment layers. At well W-3, the depth to the lower Cretaceous surface is 98 m and at W-4 is 123 m, whereas at well W-66, this depth is $>1250$ m and at W-27 is $>2000$ m (Bokov and Chemberski, 1987). Less than 10 km southeast of W-66, this depth rises to 3615 m (W-59). We estimate that depth to high-density strata increases by a factor $>10$, going from the western elevated horst structure to the eastern depression.

Core samples from wells in the Dolna Kamchia depression show a significant difference in the density of tertiary-upper Cretaceous layers and lower Cretaceous-Jurassic-Triassic layers (Dachev, 1988). The weighted average density of the upper sediment complex is approximately 2.42 g/cm$^3$ (2420 kg/m$^3$). The lower complex shows densities from 2.63 to 2.68 g/cm$^3$ at a good average density of 2.65 g/cm$^3$; thus, the density contrast between these two main sediment complexes is approximately 0.23 g/cm$^3$ (230 kg/m$^3$).

The Bouguer gravity profile and the calculated first derivatives across the gradient axis are shown in Figure 6. The profile lies between wells W-3 and W-66 (Figure 5). The steep gradient zone is long enough to allow the interpretation model to be considered as a 2D model of a contact structure. The gravity profile is 15.875 km long with 0.125 km of spacing between the sampled data points. The field drops from 29 to 5 mGal on average from west to east. The gravity anomaly, $\Delta g$, contains a background $b$ of 5 mGal and local anomaly $g$ with an amplitude of approximately 24 mGal. The horizontal derivative, $\partial\Delta g/\partial x$, has its principal extremum of $(-8.87)$ mGal/km at $x = 5.875$ km, where the vertical derivative $\partial\Delta g/\partial z = 0$ and $\Delta g = 18.65$ mGal; hence, we assign $x_0 = 5.875$ km for the upper edge point of the thick contact structure. The vertical derivative, $\partial\Delta g/\partial z$, shows its main extrema at $x = 4.875$ and 7.625 km. Possible thin steps in the complicated fault zone appear at $x = 4.500$ and 7.375 km.

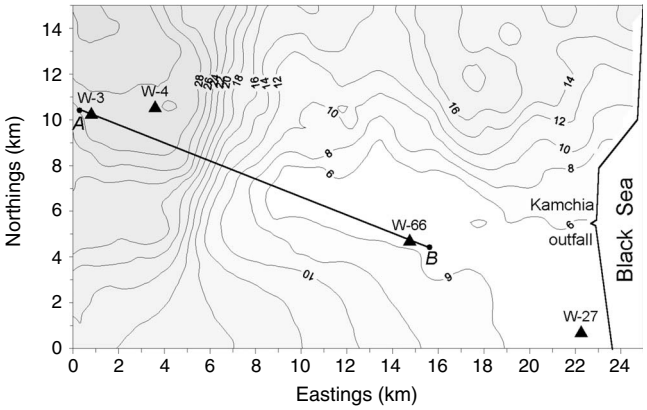


Figure 5. Fragment of the anomalous gravity field $\Delta g$ in the area of the Dolna Kamchia depression. $A$ and $B$, first and end points of the inverted gravity profile across the Venelin-Aksakov gravity gradient zone; W, wells near the profile.

The geologic data discussed here strongly suggest that this is a contact of considerable depth extent. The same follows from the estimation of parameter $p = z_2/z_1$, whose value, estimated from equation 16, for $|\partial\Delta g/\partial x|_e = 8.87$ mGal/km and $\rho = 0.23$ g/cm$^3$, is equal to 18. For the possible contrast densities between 0.20 and 0.26 g/cm$^3$, this parameter varies between 27 and 13, keeping high values suitable for testing our formulation.

Using the method described here, we should compose equation system 10 in a series of windows centered at $x_0 = 5.875$ km. We take the same windows for the solution of system 13. The use of equation set 14 needs the contact edge, $x_0$, and the density contrast $\rho$ as input. The known density contrast is close to 0.23 g/cm$^3$.

The results from equations 10, 13, and 14, using positive degree of homogeneity $n = 1$ or negative SI $N = -1$, are shown in Table 2. The tests are in order of their increasing window length from 2 to 4 km with a step of 250 m.

The estimated coordinate $x_{0e}$ of the contact edge point decreases systematically, except for window test 4, where it falls very close to the point of maximum horizontal gravity gradient.

The estimated depth $z_{1e}$ to the upper edge point of the contact model varies from 0.154 to 0.618 km. The latter result is obtained for the shortest length window (test 1), which covers a segment of the vertical gravity derivative $\partial\Delta g/\partial z$ quite close to linear (Figure 6).

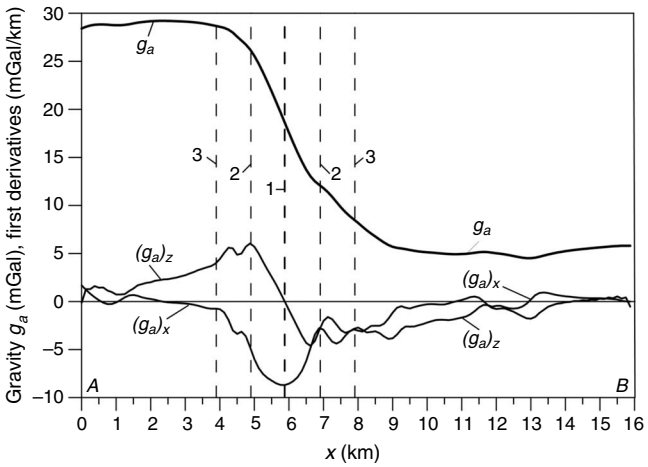


Figure 6. Anomalous gravity profile $g_a$ from point A to point B (Figure 5) and calculated horizontal derivative $(g_a)_x = \partial(g_a)/\partial x$ and vertical derivative $(g_a)_z = \partial(g_a)/\partial z$. Lines: 1 — at estimated horizontal location $x_0$ of the upper edge point of the Venelin-Aksakov fault structure and at center point of the data windows $W$; 2, boundaries of the narrowest data window for Euler deconvolution; 3, boundaries of the widest data window.

**Table 2. Estimated parameters of the Venelin-Aksakov fault from the solution of systems of equations 10 and 13 and from equation 14 for the Kamchia gravity profile in Figure 5.**

| No. test | Window from $x_1$ to $x_2$ (km) | Location of edge $x_{0e}$ (equation 10) (km) | Depth $z_{1e}$ (equation 10)/$z_{1e}$ (equation 13) (km) | Average depth $z_{1e}$ (km) | Density $\rho_e$ (equation 10)/$\rho_e$ (equation 13) (g/cm$^3$) | Average density $\rho_e$ (g/cm$^3$) | Average depth (equations 10, 13, and 14) |
|---|---|---|---|---|---|---|---|
| 1 | 4.875–6.875 | 5.820 | 0.754/0.714 | 0.734 | 0.500/0.478 | 0.489 | 0.618 |
| 2 | 4.750–7.000 | 5.771 | 0.505/0.428 | 0.466 | 0.393/0.357 | 0.375 | 0.440 |
| 3 | 4.625–7.125 | 5.758 | 0.297/0.231 | 0.264 | 0.305/0.278 | 0.291 | 0.305 |
| 4 | 4.500–7.250 | 5.764 | 0.140/0.083 | 0.112 | 0.239/0.219 | 0.230 | 0.203 |
| 5 | 4.375–7.375 | 5.745 | 0.056/0.018 | 0.037 | 0.205/0.182 | 0.193 | 0.154 |
| 6 | 4.250–7.500 | 5.680 | 0.045/0.077 | 0.061 | 0.201/0.169 | 0.185 | 0.170 |
| 7 | 4.125–7.625 | 5.612 | 0.083/0.084 | 0.084 | 0.216/0.177 | 0.197 | 0.185 |
| 8 | 4.000–7.750 | 5.570 | 0.128/0.058 | 0.093 | 0.231/0.194 | 0.212 | 0.191 |
| 9 | 3.875–7.875 | 5.550 | 0.148/0.038 | 0.093 | 0.237/0.205 | 0.221 | 0.192 |

The results shown from equation 13 correspond to the edge coordinate $x_0 = 5.875$ km as input. The same coordinate $x_0$ and density contrast $\rho = 0.230$ g/cm$^3$ are input for the calculation of minimal $z_{1e} = 0.388$ km from equation 14.

This will not lead to a stable system of equations. The estimated depth decreases with the window widening up to test 5, where it is wider than the distance between the two extrema of the calculated derivative $\partial\Delta g/\partial z$. After this test, the estimated depth shows a moderate increase with the window width. The wider window of test 9 includes the effects of the adjoining two smaller steps. Their influence on the results seems to be weak.

The values of the estimated average density contrast $\rho$ show similar behavior to that of the depth $z_{1e}$. Test 1, with the narrowest window, gives the maximum average value of 0.489 g/cm$^3$. This is consistent with the coupling effects between thickness and density contrast discussed already. The minimum contrast of 0.185 g/cm$^3$ appears for window test 6. With widening window, the estimated density contrast increases to 0.221 g/cm$^3$.

We compare the results with the known geology. The average density contrast is 0.23 g/cm$^3$, as mentioned above, so we may concentrate on inversion results around this value. The estimated density contrast of 0.489 g/cm$^3$ from test 1 is unreliable for good reason (profile segment too linear) and, therefore, so is its depth of 0.618 km. We downgrade tests 2, 3, 5, 6, and 7 because their density estimates are far from the known value. That leaves tests 4, 8, and 9, for which the estimated density contrasts are 0.229, 0.212, and 0.221 g/cm$^3$, respectively. The estimated average depths of 0.203, 0.191, and 0.192 km, respectively, are well clustered, so we accept 0.195 km as the depth of the upper edge point of the Venelin-Aksakov fault structure. This is consistent with the known depths of 0.093 and 0.128 km for the strong density boundary between tertiary-upper Cretaceous and lower Cretaceous layers at wells W-3 and W-4, which are 5 and 3 km, respectively, west of the fault structure.

From the gravity anomaly with amplitude $T = 24$ mGal (Figures 5 and 6) and density contrast $\rho = 0.23$ g/cm$^3$, we estimate the depth $z_2$ to the lower edge point of the contact using the Bouguer slab approximation (e.g., Telford et al., 1990), yielding $z_2 = z_1 + T/(41.9\rho) = 2.690$ km. This result is also consistent with the known depths to the upper surface of dense lower Cretaceous in the Dolna Kamchia depression.

The field example demonstrates the use of the positive degree of homogeneity or the negative SI in Euler deconvolution using our modified formulation. The coordinates of the upper edge point of a gravity contact/fault structure with a significant depth extent can be estimated with acceptable accuracy.

## CONCLUSION

Our revised formulation of Euler deconvolution using all variables of dimension length has been demonstrated on a model and on a field example, applying a positive degree of homogeneity corresponding to the extended negative SI $N = -1$. It is useful for gravity fault structures with considerable depth extent. The method most easily estimates the upper singular point of the gravity contact model. When we have good density data, we obtain improved stability and uniqueness of the inversion. Successfully locating the upper edge point is the key to the estimation of all parameters of the fault structure, especially the depth to the lower edge point of the structure.

## ACKNOWLEDGMENTS

We greatly appreciate the helpful comments of the editors Michal Ruder and Jose Carcione and reviewers Afif Saad, Martin Mushayandebvu, and Richard S. Lu.

## REFERENCES

Barbosa, V. C. F., J. B. C. Silva, and W. E. Medeiros, 1999, Stability analysis and improvement of structural index estimation in Euler deconvolution: Geophysics, **64**, 48–60.
Bokov, P., and Ch. Chemberski, eds., 1987, Geological preconditions for the oil and gas bearingness in North-East Bulgaria: Technika.
Courant, R., and F. John, 1965, Introduction to calculus and analysis: Wiley Interscience.
Dabovski, C., I. Boyanov, Kh. Khrischev, T. Nikolov, I. Sapunov, Y. Yanev, and I. Zagorchev, 2002, Structure and Alpine evolution of Bulgaria: Geologica Balcanica, **32**, 2–4, 9–15.
Dachev, Ch., 1988, Structure of the Earth crust in Bulgaria: Technika.
Gerovska, D., and M. J. Arauzo-Bravo, 2003, Automatic interpretation of magnetic data based on Euler deconvolution with unprescribed structural index: Computers & Geosciences, 29, 949–960.
Mushayandebvu, M. F., V. Lesur, A. B. Reid, and J. D. Fairhead, 2004, Grid Euler deconvolution with constraints for 2D structures: Geophysics, **69**, 489–496.

Nabighian, M. N., and R. O. Hansen, 2001, Unification of Euler and Werner deconvolution in three dimensions via the generalized Hilbert transform: Geophysics, **66**, 1805–1810.
Reid, A. B., J. M. Allsop, H. Granser, A. J. Millet, and I. W. Somerton, 1990, Magnetic interpretation in three dimensions using Euler deconvolution: Geophysics, **55**, 80–91.
Reid, A. B., D. FitzGerald, and P. McInerny, 2003, Euler deconvolution of gravity data: 73rd Annual International Meeting, SEG, Expanded Abstracts, 576–579.
Salem, A., and D. Ravat, 2003, A combined analytic signal and Euler method (AN-EUL) for automatic interpretation of magnetic data: Geophysics, **68**, 1952–1961.
Stavrev, P., 1997, Euler deconvolution using differential similarity transformations of gravity or magnetic anomalies: Geophysical Prospecting, **45**, 2, 207–246.
Stavrev, P., and A. B. Reid, 2007, Degrees of homogeneity of potential fields and structural indices of Euler deconvolution: Geophysics, **72**, no. 1, L1–L2.
Telford, W. M., L. P. Geldart, and R. E. Sheriff, 1990, Applied Geophysics, 2nd ed: Cambridge University Press.
Thompson, D. T., 1982, EULDPH — A new technique for making computer assisted depth estimates from magnetic data: Geophysics, **47**, 31–37.
Tikhonov, A. N., and V. Y. Arsenin, 1977, Solutions of ill-posed problems: Winston and Sons.
Zhang, Ch., M. F. Mushayandebvu, A. B. Reid, J. R. Fairhead, and M. E. Odegard, 2000, Euler deconvolution of gravity tensor gradient data: Geophysics, **65**, 512–520.
Zhdanov, M. S., 2002, Geophysical inverse theory and regularization problems: Elsevier Science Publishing Co.